Sustainable Energy & Fuels

ROYAL SOCIETY OF CHEMISTRY

PAPER

Cite this: *Sustainable Energy Fuels*, 2022, **6**, 2553

Birnessite-clay mineral couple in the rock varnish: a nature's electrocatalyst†

Amritpal Singh Chaddha, [ab] Narendra Kumar Singh, *[a] Manisha Malviya[c] and Anupam Sharma*[b]

Hydrogen (H_2) energy is produced by electrochemically splitting water molecules, and if produced economically, it will bring a paradigm shift in the development of sustainable energy systems. Several attempts have been undertaken in recent years to produce better electrocatalysts for the water oxidation process, with a focus on oxygen evolution reaction (OER) processes. A lot of work has gone into designing effective manganese-based heterogeneous catalysts for the water oxidation process, and a number of synthesized manganese oxides have been shown to have good alkaline OER activity. With the first-ever description of a natural material (rock varnish) constituted of birnessite (δ-MnO_2) combined with clay minerals as a potential OER catalyst, the current work represents a typical scenario of the marriage between energy and the environment. This natural material having a current density of 10 mA cm^{-2} at a lower overpotential (η) of 312 mV and a Tafel slope of 46 mV dec^{-1} exhibits exceptional electrocatalytic performance on par or better than its synthesized Mn-based electrocatalysts. Rock varnish paves the way for developing highly active as well as stable manganese-based water oxidizing catalysts and may serve as a model for the biomimetic inspired synthesis of novel classes of MnO_2-clay based composite materials as efficient water electrocatalysts for our future clean energy needs.

Received 10th February 2022
Accepted 13th April 2022

DOI: 10.1039/d2se00185c

rsc.li/sustainable-energy

1. Introduction

Rock varnishes are the dark, brown-coloured natural micro-coatings found on rocks in dry and semi-arid regions around the world.[1] These black-brown veneers are often made up of Fe and Mn oxides mixed with clay minerals,[2] and they form on the rock surfaces over time as a result of various environmental and chemical processes.[3] These enigmatic coatings have always been employed to create petroglyphs and have piqued the interest of archaeologists. Geologists, on the other hand, are always interested in learning more about how these varnish layers originate, examining their characteristics, and even assessing their paleoclimatic significance.[4] The abiotic hypothesis, which holds that small changes in pH can concentrate manganese in these layers *via* geochemical processes,[5] and the biotic hypothesis, which holds that bacteria and other microorganisms are responsible for manganese concentration,[6] have been proposed to explain the origin of rock varnishes. As a result, rock varnishes have kindled the curiosity of archaeologists and geologists working in various geographical locations around the world.[7,8]

Research on the mineral composition and geochemical analysis of rock varnishes have been published worldwide, but only a few studies on the semiconducting characteristics of these Fe/Mn oxide coatings have been reported.[9] Although manganese oxide is an abundant natural resource and is a low-cost material,[10] the electrochemical applications of manganese oxide present in the varnish layer have been overlooked. Manganese oxides occur naturally in both crystalline and amorphous forms, with MnO_6 octahedral units being found in the corners of crystalline layered or tunnelled formations.[11] The enormous surface area and porosity of these structural designs are advantageous in a range of applications, including heterogeneous catalysis, hazardous waste clean-up, rechargeable batteries, and supercapacitor production.[12]

Alternative energy sources are not a new concept for humans; however, energy has become the world's most important concern in the 21st century. Fossil fuel supplies are limited, and they are expected to be consumed by the middle of this century.[13] Particularly, when there is a push to reduce CO_2 emissions to alleviate the negative impacts of global warming, the search for alternate and clean energy resources has accelerated. Alternatively, processes, such as photocatalytic water splitting, have also been proposed as a possible technique for producing clean hydrogen from solar energy.[14,15] As a result of this debate, hydrogen generation has emerged as a vital

[a]*Department of Chemistry, Faculty of Science, University of Lucknow, Lucknow-226007, India. E-mail: nksbhu@yahoo.com*

[b]*Birbal Sahni Institute of Palaeosciences, 53 University Road, Lucknow-226007, India. E-mail: anupam110367@gmail.com*

[c]*Department of Chemistry, Indian Institute of Technology (BHU), Varanasi-221005, India*

† Electronic supplementary information (ESI) available. See https://doi.org/10.1039/d2se00185c

component of our future energy systems,[16] as hydrogen and oxygen produced by water oxidation have no negative environmental impact.[17] However, successful water electrocatalysis necessitates a low electrical energy consumption in the electrolytic cell, which is difficult to achieve.[18] This is accomplished by employing appropriate electrocatalysts, and the search for materials that can reduce both anodic and cathodic overpotentials has accelerated.[19]

The electrochemical water splitting oxygen evolution process (OER) is a source of hydrogen energy. The metal oxide-based electrocatalysts utilized in this method, such as RuOx and IrOx have high activity for OER,[20] though they are less cost-effective. On the other hand, perovskite as electrocatalysts also exhibits promising catalytic activity.[21–23] Therefore the development of low-cost, widely available metal-oxide-based electrocatalyst is required, which has led to the creation of a number of manganese-oxide-based electrocatalysts.[24] Several Mn-oxide-based compounds, such as nanoflakes, nanosheets, nanowires, and nanoflowers, have been generated as OER electrocatalysts in a variety of morphologies with considerable surface areas.[25] As a result, the entire MnO_2-based family of compounds has shown promising catalytic activity in alkaline as well as neutral media oxygen evolution reactions.[26–34]

The current study discloses a novel application of nature's substance, rock varnish, as an electrocatalyst in water electrocatalysis, keeping in mind the broad electrocatalytic applications of synthesized MnO_2-based materials. Manganese oxide (δ-MnO_2) is found in the natural matrix of other silicate minerals, as well as clay minerals, in rock varnish. When compared to other classes of synthesized Mn oxide compounds, various spinels[35–39] and perovskite oxides,[40,41] our material exhibits progressing performance, making it a great and promising avenue for the synthesis of a new generation of MnO_2-clay type composite materials for energy applications.

2. Methods

2.1 Physicochemical characterisation

2.1.1 FE-SEM-EDS. The surface morphology and elemental composition of the rock varnish sample, scrapped varnish layer, and host rock coated on bare Ni and Pt plates were examined using a field emission scanning electron microscope, which is coupled with energy dispersive X-ray spectroscopy (FESEM-EDS, JEOL JSM-7610f).

2.1.2 XRD. At ambient temperature, the X-ray diffractometer (PANalytical Xpert4'3 Powder) with an irradiance of Cu Kα1 = 1.540598 Å; Kα2 = 1.544426 Å, produced an X-ray diffraction pattern of the scrapped powdered varnish sample using a Brag–Brentano geometry on a silicon substrate zero background holder. At generator settings of 30 mA, 40 kV, the pattern was observed from 5° to 70° in the 2θ range (step size ($^\circ 2\theta$) = 0.0130, scan time = 32 s per step). Rietveld refinement[42] was performed on the obtained birnessite-type material present in the varnish layer using high score software.[43] Vesta software[44] was used to create the polyhedral crystal structure depiction and simulated diffraction pattern.

2.1.3 ED-XRF. Micro-X-ray fluorescence was used to determine the elemental make-up of the varnish layer and the host rock sample (Model: Bruker Artax 200). In the helium atmosphere, XRF scans were recorded for five distinct places in the varnish layer and the host rock with a live time of 300 s. The molybdenum X-ray tube's maximum operating voltage and current were 50 kV and 700 A, respectively.

2.1.4 Raman spectroscopy. Using a coherent argon ion (Ar^+) laser at a power of 1% with a 488 nm wavelength, Raman spectroscopic examination was performed on two separate places of the surface of the varnish layer and the host rock. The spectra were acquired using a RENISHAW *via* Reflex Raman microscope spanning a range of ~200 to ~2000 cm^{-1} with an exposure time of 30 s. The Raman signal for Si acquired from the internal silicon wafer reference at 520 cm^{-1} was used to calibrate the instrument.

2.1.5 Infrared spectroscopy. An FTIR spectrophotometer (Agilent Technologies Carry 630) with a diamond crystal in the range of 400 cm^{-1} to 4000 cm^{-1} was used to investigate the material's distinctive functional groups.

2.1.6 WD-XRF. Elemental measurement for key elements was performed using a wavelength dispersive X-ray fluorescence (WD-XRF) spectrometer (Model: PANalytical, axios max, 4 kW). The fusion bead method was used to determine the varnish layer concentration of major oxides by taking 0.5 g of scrapped varnish sample with 4.85 g lithium tetraborate and 1.20 g lithium carbonate and then fusing it above 1000 °C in a platinum crucible with lithium iodide as wetting agent. After fusion, fused mass was transferred to Pt–Au mould to give the shape of disc precession and accuracy was 2 percent (using GSS, GSD, and other rocks standards).

2.2 Electrochemical characterisation

2.2.1 Electrode fabrication and electrochemical measurement. A varnish layer and the host rock (the substrate on which the varnish is formed) were used to create mineral electrodes. The varnish layer is scrapped from the host rock with a diamond-coated coarse bit on a micro drill (Model no. 800 Dremel) and ground into fine powder in an agate mortar. A vibratory disc mill was also used to powder host rock (Model no. Retsch RS200). A powdered varnish sample (40 mg) was mixed with 5% Nafion solution (20 μL) and anhydrous ethanol (400 μL) to prevent the electrode material from shedding. The mixture was then applied to one side of Ni and Pt pre-treated conductive support to create a varnish coating on the electrodes, followed by the same process on the host rock.[45,46] A conventional three-electrode system was used[9,47,48] in the study. The working electrode was made from varnish and host rock film, while the reference and auxiliary (counter) electrodes were made from Hg/HgO in 1 M KOH (E° = 0.098 V *vs.* NHE) and pure Pt-foil with a large geometrical surface area (~2 cm^2), respectively. To reduce the solution resistance (*iR* drop) between the working electrode and the cell solution, the reference electrode was connected to the cell solution *via* the Luggin capillary (the KCl/agar–agar salt bridge). An electrochemical workstation (Gamry Reference 600 ZRA) equipped with a potentiostat/galvanostat was used to monitor the potential of the working (test)

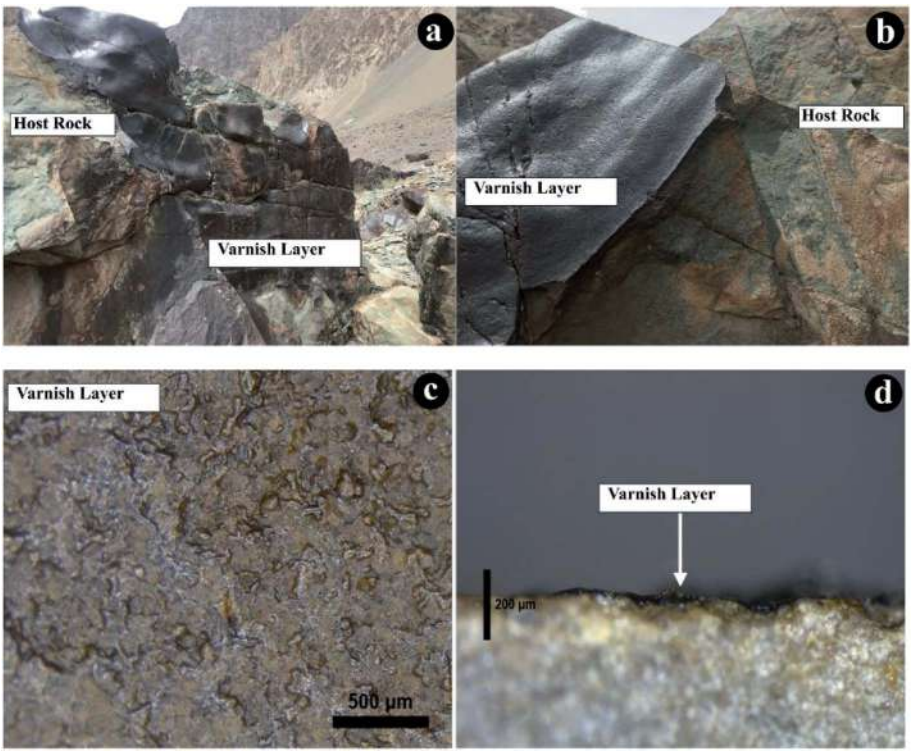

Fig. 1 (a) Synoptic view of varnish coated rock boulders in the field; (b) close-up photograph of the boulder displaying dark rich varnish coated onto the host rock; (c) microscopic image of top varnish layer; (d) cross-sectional view of varnish sample under an optical microscope.

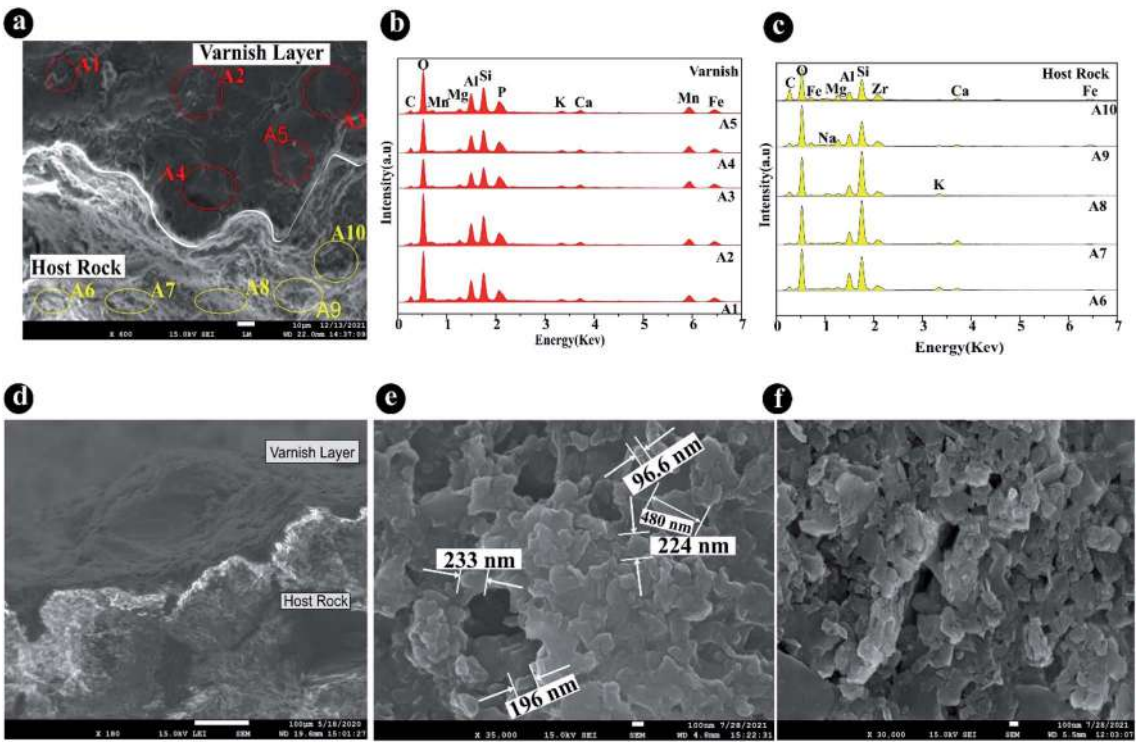

Fig. 2 (a–c) Multi-area (A1-A10) EDS analyses of the rock varnish layer and the host rock reveal a significant difference in the elemental composition; (d) BSE image of the rock varnish sample taken with an FE-SEM at 180× magnification. The boundary between the varnish layer and the host rock is demarcated; (e and f) surface morphology of the rock varnish sample at 350 00× magnification images reveal clusters of different size particles and nanoflakes-like morphology.

electrode in relation to the reference electrode. The cyclic voltammogram (CV) and anodic polarization studies were carried out using corrosion and physical electrochemistry software. All measured potentials were calibrated and converted to the reversible hydrogen electrode (RHE) by utilising $E_{(RHE)} = E_{(Hg|HgO)} + 0.0591 \times pH + 0.098$ V,[49] where $E_{(Hg/HgO)}$ is the observed potential *vs.* Hg/HgO, pH is measured to be 13.44 for the 1 M KOH electrolyte, and $E^0_{(Hg/HgO)}$ is 0.098 V for Hg/HgO. Using electrochemical impedance spectroscopy (EIS), the electrochemically active surface area (ECSA) was calculated in terms of roughness factor (R_F). The CHI 608C instrument is used to record the ac-impedance spectra in the frequency range 0.01–100 kHz at a certain dc-potential (100 mV). The electrode/electrolyte interface was measured using the simplest equivalent circuit model, which consisted of solution resistance (R_S) in series with polarization resistance (R_P) and parallel to capacitance (C) (Fig. S13†).

3. Results and discussion

3.1 Physicochemical characterization

Rock varnish samples were chipped out of large rock boulders ~80–40 Ma old[50,51] from the high-altitude, extreme environmental, and cold desert region of Ladakh, India (Fig. 1a and b). Brown varnish layer microscopic analysis reveals that the varnish layer thickness varies from millimetres to submicron and is present as a coating on the host rock (Fig. 1c and d). The surface morphology of the varnish layer and the host rock differ significantly, according to FE-SEM/EDS analysis with BSE image (Fig. 2a). The multi-area elemental analysis also reveals that the varnish layer has a higher Mn content than the host rock (Fig. 2b and c). Birnessite-like particles forming many clusters of several hundred nanometres are also seen in the rock varnish sample[52] (Fig. 2e). Natural birnessite has poorly crystalline structures (δ-MnO_2) with non-defined multiple aggregates of tiny particles, according to the surface morphology of varnish.[53] The particles are arranged in a nanoflakes-like geometry in the varnish layer, which looks to be very similar to the synthesized MnO_2 nanoflakes[54] (Fig. 2f).

Manganese and iron minerals cause a significant background due to unwanted fluorescence phenomena in mineralogical examinations of varnish surfaces, obscuring the detection of mineral peaks.[55] Furthermore, the varnish layer is made up of manganese and iron oxides that are fused with clay minerals, quartz, and other silicates, making mineral phase identification challenging.[56] The birnessite (δ-MnO_2) phases revealed in the layer, along with the aluminium silicate (albite) and quartz in the varnish sample, were not sharp, but rather found to be nano-crystalline, which complements the morphology of the Mn-oxide particles observed in electron microscopy. Signature peaks in birnessite were observed in the sample,[57–59] at $d = 7.1$ Å (0 0 1) and $d = 3.5$ Å (0 0 2), providing practical measurements of the birnessite interlayer. Other phases at $d = 2.4$ Å (1 1 –1), 2.1 Å (1 1 −2) and 1.8 Å (2 0 2) matched with JCPDS card no. 43-1456. Quartz along with aluminium silicate (albite) was also present in the varnish matrix[60] (Fig. 3a). The other phases contained in the varnish layer were validated using crystallographic information files

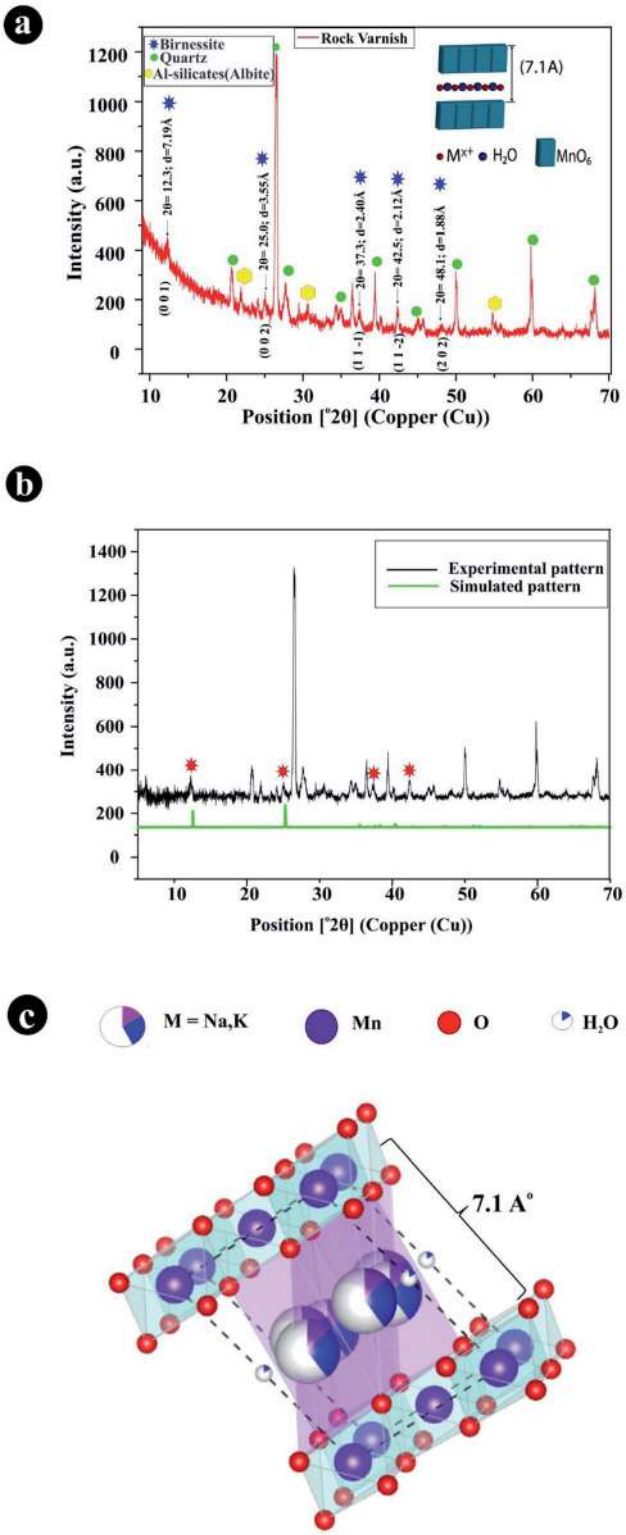

Fig. 3 (a) XRD diffractogram showing the mineralogy of varnish layer; (b) comparison plot of the simulated powder diffraction pattern of varnish sample with the experimental diffractogram; (c) polyhedral crystal structure of birnessite (δ-MnO_2) present in varnish layer produced using the Vesta software.

Table 1 Structural data obtained after Rietveld refinement of birnessite phase in the varnish layer

Lattice parameters		Bond distances (Å)	
a (Å)	5.11914	Mn–Mn (interlayer)	7.18
b (Å)	2.81155	Mn–O1 (bridged)	1.93
c (Å)	7.17809	Mn–Mn (intralayer)	2.921
α (°)	90	Mn–O1 (terminal)	1.91
β (°)	101.2862	Mn–H_2O	3.589
γ (°)	90	Mn–K	3.956
Vol. (Å^3)	101.3146	K-H_2O	1.457
Crystal system	Monoclinic		
Point group	$2/m$		

from COD IDs 96-900-1632 (albite) and 96-900-9667 (quartz). Additionally, Rietveld refinement plots were included along with the crystal structures and refined lattice parameters (Fig. S14, S15, Tables S4, S5†) of quartz and albite, respectively. The presence of aluminium silicates as a major component in layer moiety confirms the presence of clay minerals.[61] The presence of birnessite phases in the varnish matrix was also confirmed using the crystallographic information file from COD ID: 9001272 using the open crystallography database and the AMS file from the American mineralogist crystal structure database. The simulated powder diffraction pattern (Fig. 3b) was correlated with the d_{001} and d_{002} basal plane peaks, and the polyhedral crystal structure of the birnessite (Fig. 3c) was derived using the structure refinement parameters as given in Table 1. This is the same as the birnessite materials that were previously synthesised.[57,62–64]

A Raman spectrum was obtained on a varnish coated rock sample with two micro-spots at different locations on the layer denoting RVS1 and RVS2, which depicts two primary peaks of birnessite with ν1 (~641 cm^{-1}) out-of-plane Mn–O bond stretching and the ν2 (~578 cm^{-1}) basal plane Mn–O bond stretching[59,65] linked to the MnO_6 octahedron. In the varnish layer, there is also a secondary band of birnessite at ~295 cm^{-1} (ref. 66) (Fig. 4a). The spectrum was also compared with standard MnO_x, Mn_2O_3, Mn_3O_4, and δ-MnO_2 samples (Fig. S5a and b†), which clearly substantiate the δ-MnO_2 structure in the catalyst, with the appearance of bands at ~514 cm^{-1} and ~356 cm^{-1} in RVS1 and RVS2, which may correspond to ν(K–O) vibrations of birnessite as suggested by the spectrum of standard δ-MnO_2 (Fig. S5b†), suggesting the birnessite type structure of the catalyst. In contrast, these peaks are missing in other standard MnO_x, Mn_2O_3, and Mn_3O_4 type structures (Fig. S5a†), which have only prominent Mn–O bond vibration modes around ~640 cm^{-1} to ~650 cm^{-1}. Micro-spots HRS1 and HRS2 on the host rock, on the other hand, reveal prominent peaks at ~465–466 cm^{-1} of the hallmark Si–O symmetric stretch of quartz[67] as well as other SiO_2 vibration modes at 211 cm^{-1}, 264 cm^{-1}, 265 cm^{-1}, 355 cm^{-1}, 356 cm^{-1}, and 1273 cm^{-1}, respectively.[68,69] Plagioclase minerals in the host rock vibrate at ~509–510 cm^{-1} due to oxygen atom motion along the line dissecting the Si–O–Si/Al–O–Al angle in its structure[70] (Fig. 4a). The presence of a manganese oxide type of material in the varnish layer, different from the host rock, is further confirmed

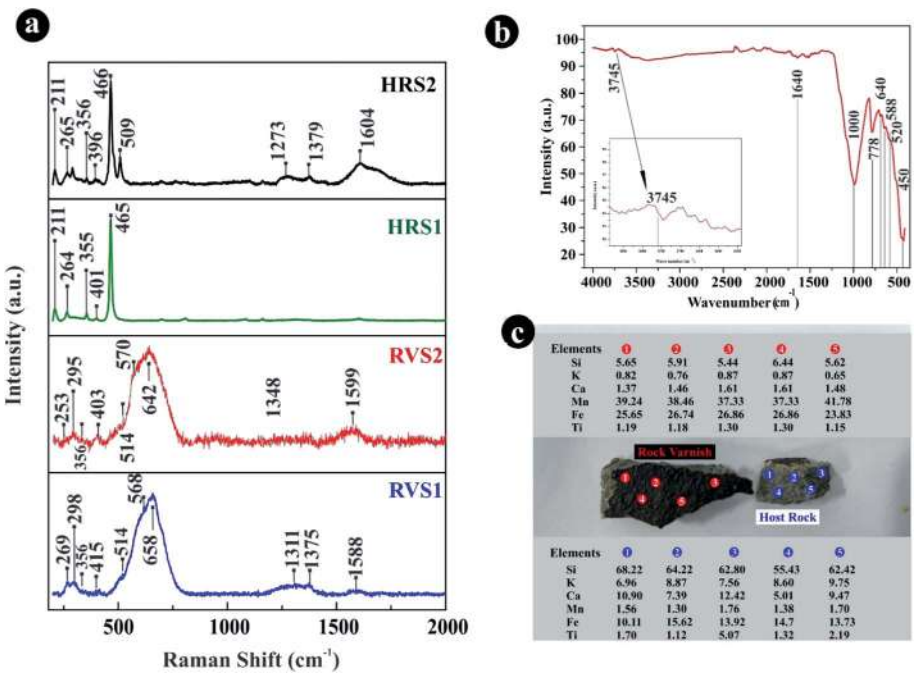

Fig. 4 (a) Multi-spot Raman examination of the varnish layer (RVS1, RVS2) and host rock (HRS1, HRS2) reveals contrast Raman spectra confirming the presence of birnessite in the layer; (b) FT-IR spectra of the varnish layer revealing characteristic peaks; (c) comparative multi-spot EDXRF analysis on five different spots on the varnish and host rock displays the percentage difference in relative elemental concentration between the varnish layer and the host rock.

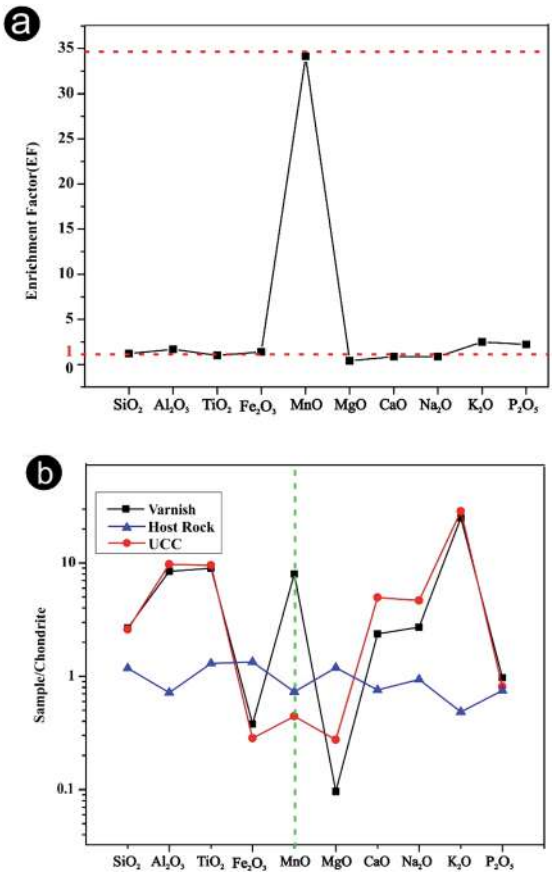

Fig. 5 (a) Diagram illustrating the enrichment factors for the primary elements in a rock varnish sample clearly revealing that Mn is significantly enriched in the varnish sample in comparison to the other elements present. (b) The chondrite normalised plot for the key elements found in the varnish and host rock depicts the relative variance in element abundance as compared to UCC (upper continental crust) values.

by the contrast between Raman peaks in the varnish layer and the host rock.

The IR spectra in this investigation reveal the functional groups present in the varnish layer and distinguish between them. Bands at ~3600–3700 cm^{-1} and ~1600 cm^{-1} correspond to stretching and bending vibrations of the –OH group of water molecules in birnessite or clay, respectively.[66,71] Mn–O stretching vibrations are represented by bands in the ~400–800 cm^{-1} range, with particular bands at ~450 cm^{-1} and 520 cm^{-1}.[72,73] Quartz signatures with primary bands at ~1000 cm^{-1} and 778 cm^{-1}, as well as second-order bands of feldspar at ~588 cm^{-1} and 640 cm^{-1}, are assigned to Si–O stretching vibrations, namely the Si–O–Si stretching vibration mode of clay minerals present in the varnish layer[74–76] (Fig. 4b).

The relative elemental concentration of Mn in the varnish layer, which increases to 39% in the layer as compared to 1.5% in the host rock, is revealed by micro-X-ray fluorescence spectrometry with simultaneous multi-elemental analysis performed on 5 different locations. A corresponding reduction in SiO_2 in the layer ~5% from ~65% in the host rock is also detected. The presence of Mn enriched material in the layer, which complements the presence of Mn-oxide type material in the varnish layer, is demonstrated by the enrichment of Mn to nearly 30 times in the layer (Fig. 4c).

To better understand the effect of elements other than Mn, which are present as impurities in the varnish layer due to its natural origin, the element concentrations (Table S3†) in the varnish layer and the host rock were determined using the WD-XRF technique by scraping the varnish layer from the host rock and analysing a homogeneous powdered sample by the pressed pellet and fusion bead method. The enrichment factor determined (Table S3†) from these results indicates a significant enrichment factor value (EF = 34) for manganese oxide when compared to the host rock (Fig. 5a), indicating a critical function for Mn in catalytic activity and minimal involvement for other elements. The interpretation of EF values is not universal, and multiple cut-off values have been employed as markers of enrichment in a certain element. In general, EF values near 1 are thought to be of crustal origin, whereas those greater than 5 are thought to be of non-crustal origin.[77] On a scale for evaluating the strength of element enrichment based on EF values, 20 < EF < 40 is regarded as being a high level of enrichment.[78]

Furthermore, the elemental concentrations of the varnish and host rock were normalised by chondrite data[79,80] (wherein chondrite provides primordial earth elemental composition) and compared with UCC[81] values, and Mn-oxide concentration in the varnish layer is clearly greater than Mn concentration in chondrite and UCC, whereas all other elements have the same abundance as the upper continental crust (Fig. 5b), indicating that elements other than Mn have a negligible effect on the varnish's catalytic activity as an electrocatalyst. On the other hand, the presence of iron in the varnish layer may improve its electrocatalytic activity by serving as reactivity facilitators or as co-catalysts in synergy with the primary catalyst material, Mn-oxide.[82]

3.2 Electrochemical characterization

The electrocatalytic activity of the materials, rock varnish and host rock (substrate), was investigated using powdered varnish film/host rock film coated on Ni/Pt conductive supports. Scanning electron microscopy was used to examine the morphology of uncoated and coated Ni and Pt supports with the materials (Fig. 6a–f). The morphological structure of the fabricated electrodes appeared to be similar to some agglomerates; the figure shows the uniform distribution of varnish and host rock particles coated onto the Ni/Pt plates. The average particle size of the milled catalyst was calculated by the sophisticated LPSA (laser diffraction particle size analyser) technique and was found to be 5 μm (Fig. S6†), with 32% of the total volume of particle size distribution (PSD) belonging to <2 μm fractions, reporting the presence of clay mineral (hydrous layered aluminosilicates) particles in the catalyst,[83] enhancing the OER activity, resulting in rapid adsorption/desorption of ions due to the high exchange capacity and pore volume of clay minerals.[84]

The redox behaviour of the rock varnish and host rock was determined by recording the cyclic voltammogram at the scan rate of 10 mV s^{-1} in 1 M KOH at 25 °C in the potential region 0.0

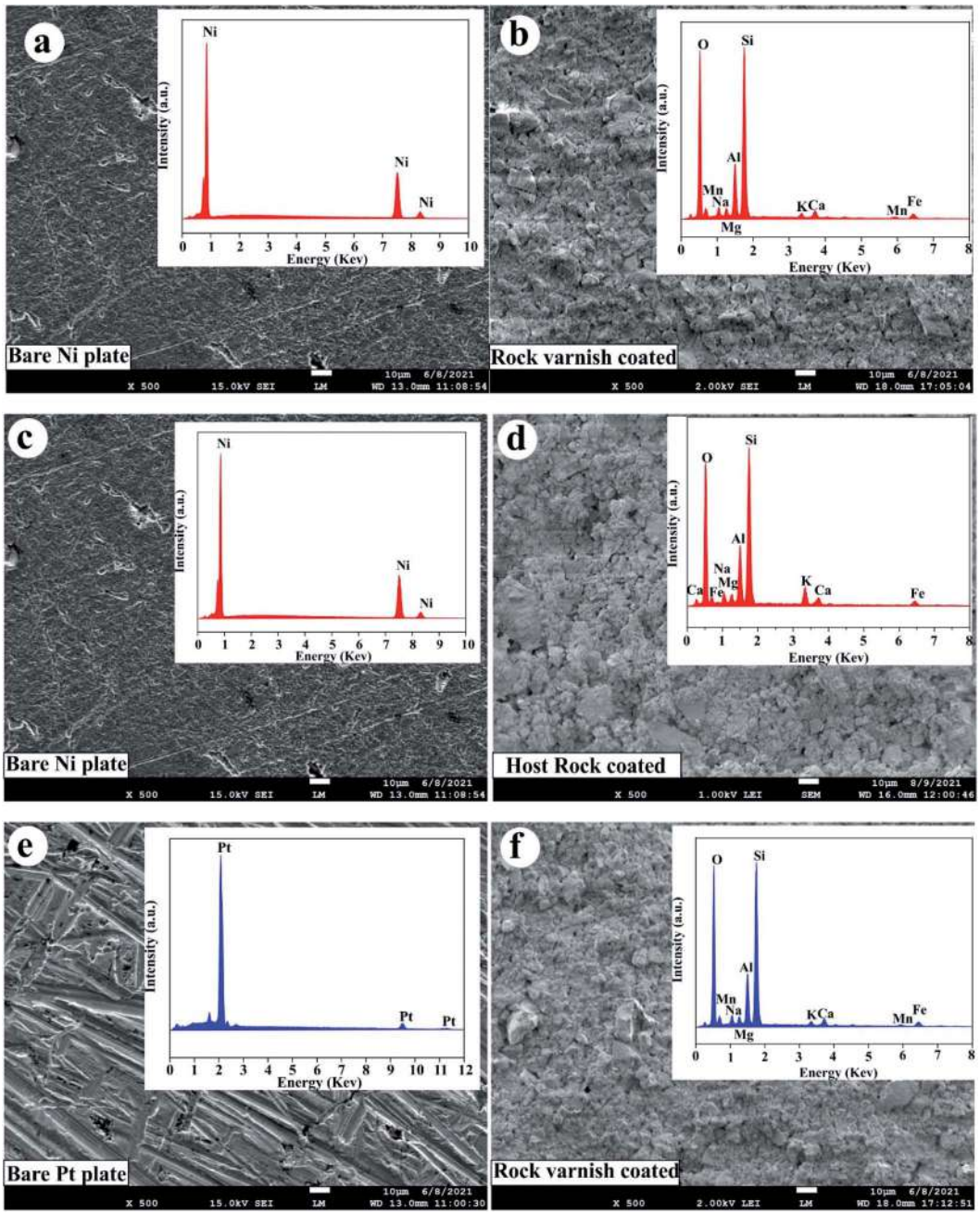

Fig. 6 SE micrographs and respective EDS spectra in the inset (a, c) bare nickel plate; (b) rock varnish powder-coated on nickel plate; (d) host rock powder-coated on nickel plate; (e) bare platinum plate; (f) rock varnish powder-coated on the platinum plate.

to 0.7 V *vs.* Hg/HgO or 0.9 to 1.6 V *vs.* RHE (Fig. 7a and b). Various parameters such as peak separation potential ($\Delta E = E_{Pa} - E_{Pc}$), formal redox potential [$E^{\circ} = (E_{Pa} + E_{Pc})/2$)], anodic peak current (i_{p_a}), and cathodic peak current (i_{p_c}) were estimated from the voltammetric curve as given in Table 2. Prior to OER, curves display anodic and cathodic peaks. The CV curves of the rock varnish and host rock are identical in form, except for their anodic and cathodic peak potential values (Table 2). Moreover, the values of anodic and cathodic peak currents in rock varnish are lower than that of the host rock (Table 2), and this variation can be attributed to the passivation of the nickel substrate by the rock varnish as a result of the adsorption–desorption of the OH^{-} ions occurring at the varnish/electrolyte interface due to the presence of clay minerals-MnO_2 amalgam present in the varnish layer, where readily exchangeable anions were being adsorbed on the exchangeable sites,[85] which is not present in the host rock owing to larger current density in the case of host rock as compared to rock varnish. However, the catalytic film remains stable during the cyclic process. The oxygen evolution reaction in rock varnish begins at a lower potential of 558 mV, whereas OER in the host rock begins at a slightly higher potential of 582 mV, indicating better efficiency towards

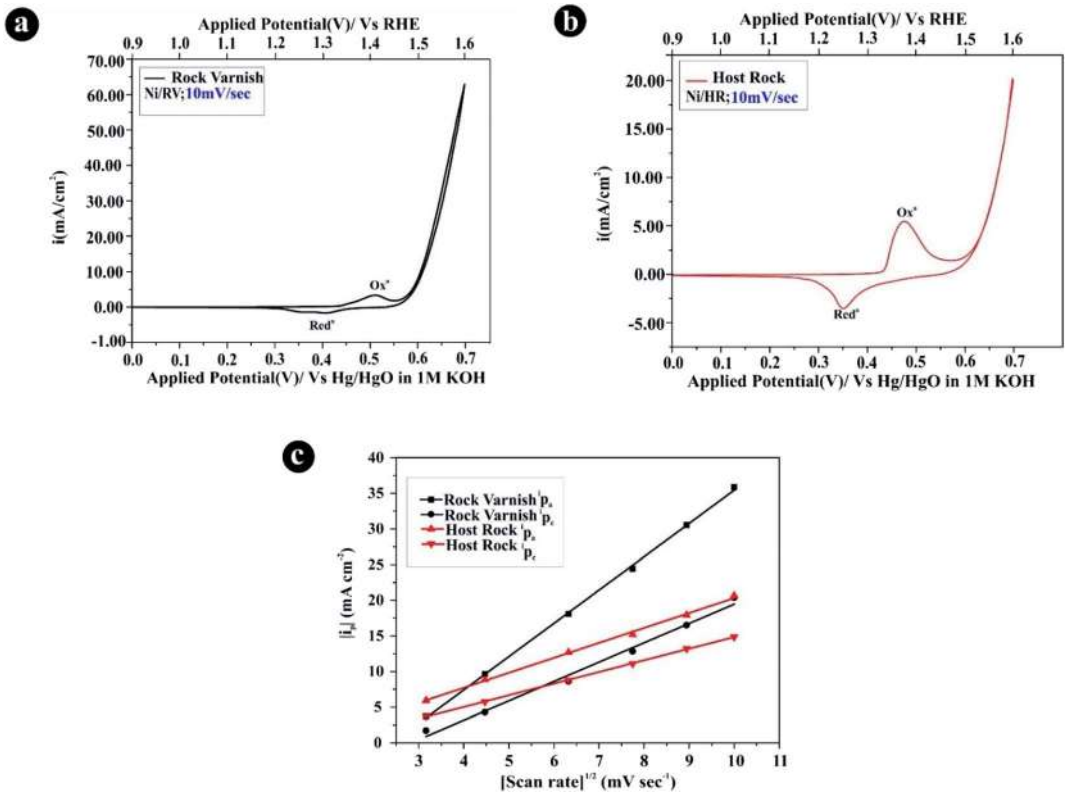

Fig. 7 (a, b) Cyclic voltammograms of the rock varnish film and host rock electrode on Ni at 10 mV s^{-1} scan rate in 1 M KOH at (25 °C); (c) plot of $|i_P|$ *vs.* (scan rate)$^{1/2}$ for the rock varnish film and the host rock film on Ni in 1 M KOH (25 °C).

Table 2 Values of the cyclic voltametric parameters in 1 M KOH at 25 °C (scan rate = 10 mV s^{-1})

Electrode	E_{Pa} mV^{-1}	E_{Pc}/mV	ΔE_P mV^{-1}	$E°$/mV	i_{P_a}/mA cm^{-2}	i_{P_c}/mA cm^{-2}	$\frac{i_{P_a}}{i_{P_c}}$
Ni/rock varnish	512	406.2	105.8	459.1	3.3	1.6	2.0
Ni/host rock	475	351.5	123.5	413.2	5.4	3.5	1.5

electrochemical processes (Fig. 7a and b), with the ratio of anodic and cathodic peak current observed to be 2.0 and 1.5 due to irreversible reaction. The CV curves obtained under analogous experimental circumstances at varied potential scan speeds between 10–100 mV s^{-1} from 0.0 to 0.65 V are quite similar to the CV curves recorded under similar experimental conditions (Fig. 7a and b). The straight line obtained in the plot of $|i_P|$ *vs.* square root of scan rate (Fig. 7c) indicates that the surface redox process is diffusion controlled.[45]

The adoption of nickel substrate as the support material in this investigation was motivated by many benefits described in prior publications,[86–91] and it was also found to be compatible with the natural material under consideration in terms of adherent support. Although Ni can operate as a pre-catalyst by providing OER sites and supporting the catalyst, the material's electrocatalytic efficiency has been supported. Noble electrodes such as Au and Pt are suitable alternatives for support in testing the material's performance; however, Au itself shows a Tafel slope of 30–40 mV dec^{-1} during the electrochemical process.[92] Pt, on the other hand, does not engage in the OER process, as revealed by isotopic studies.[93] Hence, Pt was also chosen for the comparative investigation of varnish activity and order studies (Fig. 8a and b). Additionally, the CV curve of rock varnish on Pt support recorded in the same potential region did not exhibit any redox peaks under similar experimental conditions (Fig. 9c). This suggests that the redox peaks originated from the oxidation–reduction of Ni-substrate, which undergoes contact with the electrolyte (KOH) through pores, cracks, and intercrystallite gaps.[94,95] It indicates the rock varnish's efficiency as an electrocatalyst, with its anion-exchange capacity and surface chemico-physical characteristics supporting fast hydration in an aqueous solution, culminating in wetting the whole film thickness. Tafel polarization curve in a certain potential region was determined at 0.2 mV s^{-1} of scan rate in 1 M KOH to compare the electrocatalytic activity of rock varnish on the Pt electrode (Fig. 9d). On Pt, the reaction sequence of OER was

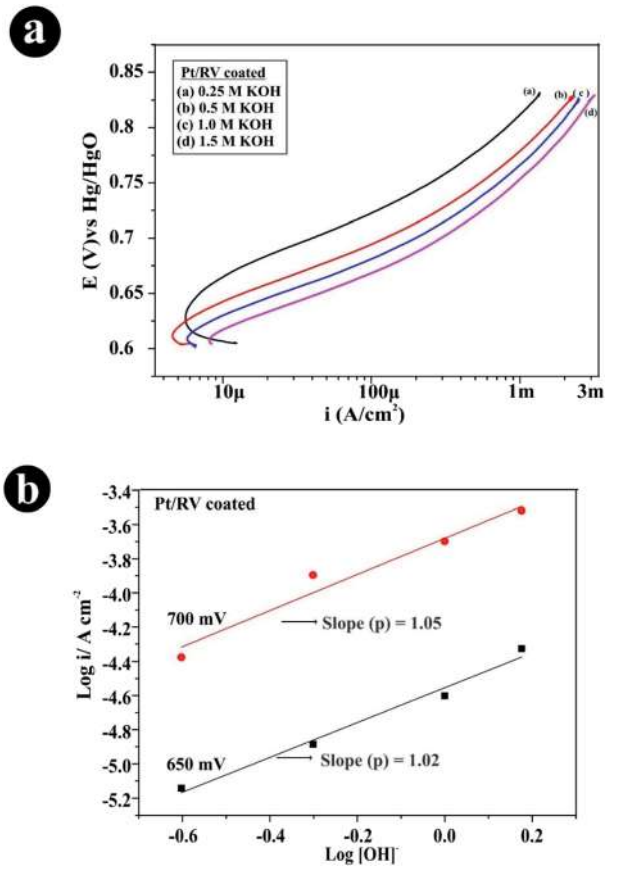

Fig. 8 (a) Tafel plots for oxygen evolution on the rock varnish on Pt at varying KOH concentrations ($\mu = 1.5$) at 25 °C; (b) plot of log *i vs.* log [OH^-] at a constant applied potential ($E = 650$ mV, 700 mV) for rock varnish film on Pt at 25 °C depicting the first order process.

established by recording the anodic polarization curve with four distinct KOH concentrations, namely 0.25 M, 0.5 M, 1.0 M, and 1.5 M (Fig. 8a). Log $_i$ at a given potential was calculated from the polarization curves and displayed against log C_{OH^-} (Fig. 8b).

3.2.1 Electrocatalytic activity. The *iR*-corrected comparative anodic Tafel polarization curves of rock varnish and host rock film electrodes on Ni at a scan rate of 0.2 mV s^{-1} in 1 M KOH at 25 °C (Fig. 12a) show a better electrocatalytic nature for the rock varnish than the host rock, respectively, in the potential region up to (1 V *vs.* Hg/HgO). The observed value of the Tafel slope reveals that both rock varnish and host rock follow similar electrochemical mechanistic paths in the lower potential region, which is close to $2(2.303RT/3F)$. Contrary to this, in the higher potential region, they follow $2(2.303RT/F)$. It is noteworthy that the Tafel slope values (46 and 49 mV dec^{-1}) obtained in the present study on both Ni and Pt electrodes coated with rock varnish, respectively (Fig. 9b and d), are similar to those found in the case of highly active Mn-based electrocatalyst materials as compared in Fig. 11.

The electrocatalytic activity was estimated from the polarisation curve in terms of the current density at overpotential (η) 450 mV. 'η' is the anodic overpotential, which is also known as the formal overpotential and is determined by the relation $\eta = E - E_{O_2/OH^-}$,[38] where, E and E_{O_2/OH^-} (=0.303 V *vs.* Hg/HgO) are the applied potentials across the electrocatalyst/1 M KOH interface and the theoretical equilibrium Nernst potential in 1 M KOH at 25 °C, respectively. The observed electrocatalytic activity of the rock varnish at 10 mA cm^{-2} is compared with the literature as given in Table 5 and found to be on par with most of the synthesized Mn-based electrocatalysts. Varnish coated on Pt electrode also shows promising results with Tafel slope of 49 mV dec^{-1} and current density of 5 mA cm^{-2} at lower overpotential (η) of 532 mV, which is superlative than the highly efficient layered manganese oxide bilayer catalyst reported earlier.[96] This demonstrates that the activity observed is attributable to the material exclusively and that Ni support does not totally operate as OER sites because the bare Pt metal has a high Tafel slope value of 162 mV dec^{-1}.[97] To normalize the material loading on the substrate, the activity was also calculated in terms of current density per mg at 450 mV. All these estimated values are listed in Table 4. The values given in the table show that the electrocatalytic activity of rock varnish is about 7 times higher than that of the host rock. The former produced $j = 15.0$ mA cm^{-2} mg^{-1} at 450 mV, while in the case of latter (host rock), it is observed as $j = 1.9$ mA cm^{-2} mg^{-1} at the same potential. This increase in the electrocatalytic property of rock varnish might be due to the presence of clay minerals in addition to oxides of Mn and Fe, as reported in a recent study.[98] As clay minerals have thin sheet silicate structures with extremely fine particle sizes and charged surfaces, the adsorption and desorption processes in clay minerals empower the adsorption of electrolytes with electrode material and thereby enhance the rate of OER. To explain the mechanism, the reaction order of OER was determined by recording the anodic polarization curve with both Ni and Pt coated electrodes (Fig. 8a and 12b, c) with four different KOH concentrations, *viz.* 0.25 M, 0.5 M, 1.0 M, and 1.5 M. The electrical intensity of each solution was kept uniform by maintaining the ionic strength constant ($\mu = 1.5$) with KNO_3 inert electrolyte. From the polarization curves, log i was estimated at a certain potential and plotted against log C_{OH^-}. The value of the reaction order, which is determined by measuring the slope of the straight line obtained in the plot of log i *versus* log C_{OH^-} (Fig. 8b and 12d), was found to be almost unity.

In order to further substantiate the findings obtained on rock varnish coated on Ni and Pt substrates, comparative electrochemical measurements on bare Ni and bare Pt substrates were obtained (Fig. 9a–d). The nature of CV of both bare Ni and Pt is the same as that of coated substrates. However, the oxygen evolution reaction in rock varnish coated on a Ni substrate begins at a lower potential of 558 mV, whereas the OER in a bare Ni electrode begins at a slightly higher potential of 650 mV, indicating the materials' better efficiency towards electrochemical processes. Clearly coated electrodes show better OER current at 1.6 V (*vs.* RHE) when compared to bare electrodes (Fig. 9a, c, S4a†). Furthermore, the comparative activity of bare substrates (Ni and Pt) was observed, with higher Tafel slope values of 91 mV dec^{-1} and 132 mV dec^{-1}, respectively (Fig. 9b and d). The electrocatalytic activity of the bare Ni electrode was 33 mA at an overpotential of 450 mV, whereas the activity of the

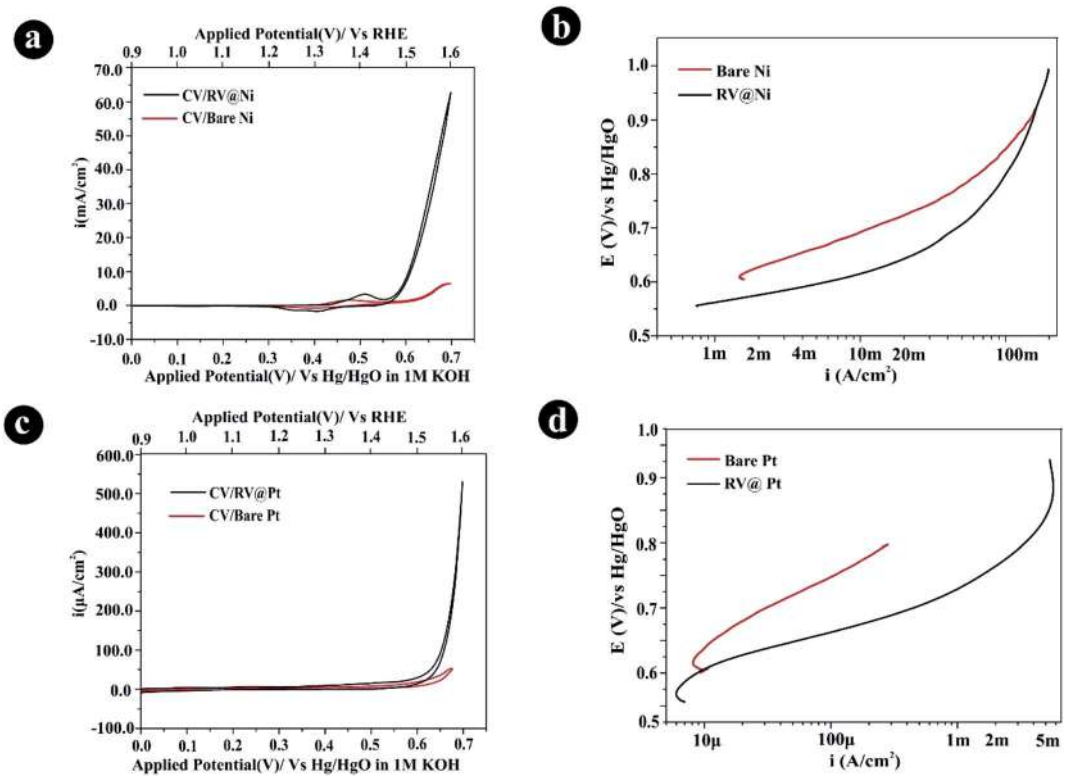

Fig. 9 (a) Comparative cyclic voltammograms of the bare Ni and rock varnish coated Ni electrodes in 1 M KOH at (25 °C); (b) Tafel plots correlating oxygen evolution on the bare Ni and rock varnish coated Ni electrodes at 25 °C in 1 M KOH; (c) comparative cyclic voltammograms of the bare Pt and rock varnish coated Pt electrodes in 1 M KOH at 25 °C; (d) Tafel plots correlating oxygen evolution on the bare Pt and rock varnish coated Pt electrodes at 25 °C in 1 M KOH.

Table 3 Comparative electrochemical characteristics of rock varnish on different substrates

	Electrodes					
	Bare Ni	RV/Ni	Bare Pt	RV/Pt	Bare GC	RV/GC
Activity at 450 mV (over potential) or 753 mV	33 mA	78 mA	114 μA	1.65 mA	14.5 μA	58 μA
Activity increase	(2.3 times the bare electrode)		~14.5 times the bare electrode)		(4 times the bare electrode)	
Tafel slope (mV dec^{-1})	91	46	132	49	93	76
Decrease of Tafel slope (mV dec^{-1})	1.9 times the bare electrode		2.7 times the bare electrode		1.2 times the bare electrode	

Table 4 Electrode kinetic parameters for OER on rock varnish and host rock in 1 M KOH at 25 °C

Electrode	Loading (mg cm^{-2})	Tafel slope (mV dec^{-1})	Order	Apparent current density i_{app} (mA cm^{-2}) at over potential (mV)	True current density i_{true} (mA cm^{-2}) at over potential (mV)	Current density (mA cm^{-2}) per mg at 450 mV (specific current density)
				450	450	
Rock varnish	5.2	46	1.1	78.0	94.0	15.0
Host rock	25.7	52	1.2	49.0	75.3	1.9

material coated on the Ni substrate was found to be 78 mA at 450 mV (Fig. 9b). Consequently, at an overpotential of 450 mV, the activity of bare Pt was found to be 114 μA, which was lower than the activity of the material coated on the Pt substrate, which used to be 1.65 mA (Fig. 9d). Additionally, electrochemical measurements were also performed on a glassy

Table 5 A comparative report with highly active Mn-oxides in 1 M KOH

		OER performance			References
Electrocatalyst	Synthesis method	KOH [M]	I (mA cm^{-2})	η (mV)	
ε-MnO_2 microspheres	Solid state reaction	1	10	420	101
α-MnO_2 nanowires@Ti foil	Electrochemical	1	—	—	26
α-MnO_2 nanosheets@Ti foil	Electrochemical	1	—	—	26
α-MnO_2@Ti foil cotton wool structure	Electrochemical	1	—	—	26
α-MnO_2 nanorods	Hydrothermal	1	10	450	27
Mn_2O_3 nanotube arrays@Ni foam	Heat treatment	1	10	270	102
Porous α-Mn_2O_3 @FTO	Electrodeposition	1	10	370	31
Porous Mn_2O_3	Electrodeposition	1	0.1	170	32
Porous Mn_3O_4	Electrodeposition	1	0.1	290	32
Mn_3O_4 nano-octahedra	Wet chemical	1	10	287	103
$CDs_{0.15}$-MnO_2 nanoskeleton–nanoflowers	Hydrothermal	1	10	343	33
Co-MnO_2 ultrathin nanosheets	Wet chemical	1	10	279	104
Co-MnO_2 nanoporous	Electrochemical deposition	1	10	400	105
(Fe,Co,Ni)-MnO_2@arbon paper ultrathin nanosheets	Electrodeposition	1	20	390	106
MnO_2-Cs^+ nanosheets	Exfoliation	1	5	613	107
α-(K)MnO_2 nanoneedles	Wet chemical method	1	10	440	108
Mn-Ni LDH nanomaterial	Wet chemical	1	10	420	109
Ni-Mn_3O_4	Coprecipitation and calcination	1	10	283	110
$NiCo_2O_4$@MnO_2 nanoneedles–nanoflakes	Hydrothermal	1	10	337	111
MnO_2@NiCoS nanoparticles@nanosheets	Hydrothermal	1	10	170	112
MnO_2/$NiCo_2O_4$ nanoparticles–nanosheets	Hydrothermal	1	10	340	113
MnO_2@Pd@C nanorods–nanoparticles-spheres	Hydrothermal	1	2.6	700	114
Mn_3O_4-$Co_xMn_{3-x}O_4$@Ni foam	Seed growth	1	10	284	115
Mn_3O_4@G-Ph-SN	Hydrothermal	1	10	473	116
N-MOF-MnO_2 composite nanoparticles–nanowires	Wet chemical method	1	10	260	117
MnO_2-CoP_3/Ti nanowires	Wet chemical	1	10	288	118
MnO_2/Ti nanowires	Wet chemical	1	10	400	119
Mn_3O_4 nanoparticles–CNTs	Wet impregnation	1	10	410	120
CoO–hi-Mn_3O_4	Chemical coupling	1	10	378	121
Rock varnish@Pt	Natural	1	5	536	*Current study
Rock varnish@Ni	Natural	1	10	312	*Current study

carbon (GC) electrode (Fig. S3, S4†). The coated GC electrode shows a similar trend to that of Ni and Pt coated varnish material, pointing towards better electrocatalytic activity. When comparing bare and coated GC electrodes, the nature of the CV curve was found to be the same in both. However, the OER current density was found to be ~3 times higher in the coated GC electrode than in the bare GC. (Fig. S4a†). Similarly, better electrocatalytic properties were observed on the coated GC substrate in comparison to the bare GC, with a lower Tafel slope of 76 mV dec^{-1} and a current density of 58 μA, whereas the latter shows a higher Tafel slope of 93 mV dec^{-1} and a current density of 14.5 μA. (Fig. S4b†). Clearly, the material shows better electrocatalytic performance when compared to bare GC. Typically, rock varnish performs better than bare electrodes in terms of electrochemical properties, with lower Tafel slope values and better electrocatalytic activity (Table 3). The influence of the substrates on OER measurements was investigated using data, as provided in Table 3, derived from anodic polarization Tafel curves for oxygen evolution on bare Ni, Pt, GC electrodes and their coated counterparts (Fig. 9b, d, S4b†). It may be established that regardless of the substrate utilized (Ni, Pt, GC), rock varnish has higher relative activity than bare electrodes. Furthermore, the sequence of OER activity is Ni@RV > Pt @RV > GC@RV. This tendency might be explained by the synergistic action of the trimetallic trio of Mn-Fe-Ni,[99] which can be attributed to the contribution of Mn, Fe from rock varnish, and Ni from the substrate, resulting in this enhanced OER performance.

The electrochemically active surface area (ECSA), *i.e.*, roughness factor (R_f) of the catalytic material film, was estimated from the double layer capacitance (C_{dl}) of the film: electrolyte interface, determined by AC impedance measurements. Fig. 10(a) and (b) represent the Bode plot for the rock

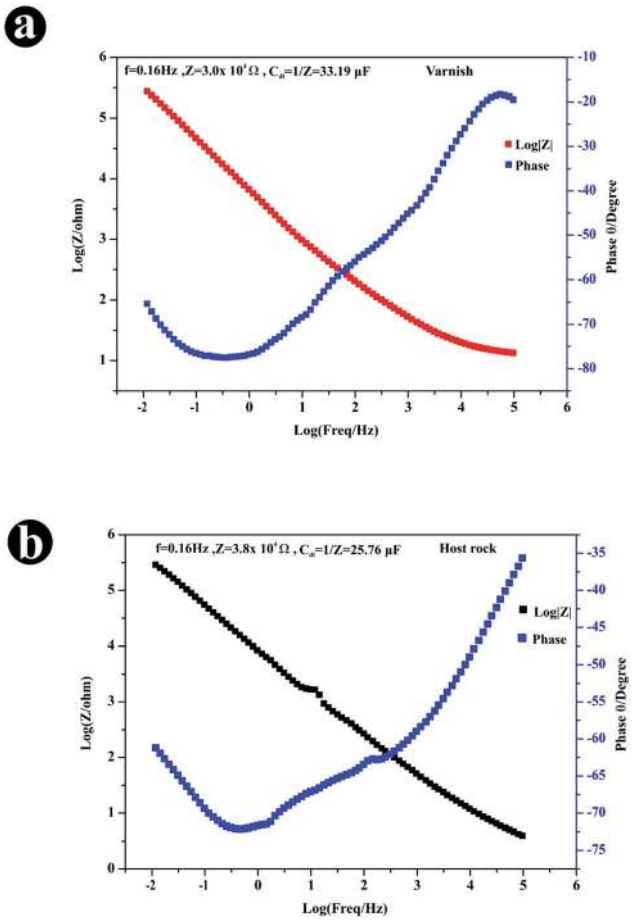

Fig. 10 (a, b) Typical Bode plot: varnish and host rock: KOH (1 M) interface at 25 °C.

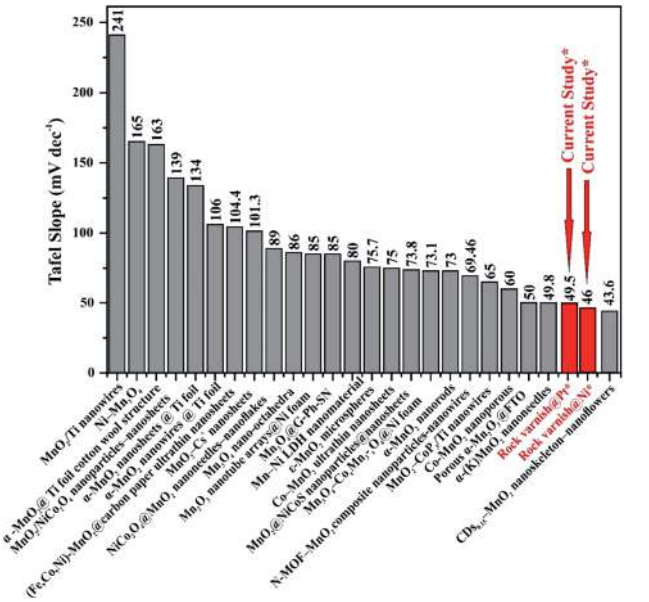

Fig. 11 Comparative chart depicting Tafel slopes of reported manganese-based electrocatalysts for water oxidation reaction with the current study.[26,27,31,33,101,102,103,104,105,106,107,108,109,110,111,112,113,115,116,117,118]

varnish and host rock, recorded in a wide range of frequency, 0.01 Hz to 100 kHz, at 100 mV. At this potential, the contribution of any faradaic process is assumed to be negligible, and ECSA (R_F) was estimated with reference to the C_{dl} (=40 μF cm^{-2}) of the smooth surface.[100] The value of C_{dl} (=1/Z) for the electrode/electrolyte interface was measured by representing the data as Bode plots log Z *versus* log f, and θ *versus* log f, and extending the linear capacitance zone to the log|Z| axis at a frequency of 0.16 Hz ($\omega = 1$). The roughness factors computed for rock varnish and host rock were 0.83 and 0.65, respectively, with a 0.8 slope value. The relatively higher ECSA value of rock varnish over the host rock clearly connects with its better electrocatalytic performance, whereas values <1 imply a bigger particle size of the material grains, which is complemented by SEM morphological examination of particle size (Fig. 2e and f) due to its natural origin.

3.2.2 Thermodynamic properties. To know the effect of temperature on OER, electrodes of rock varnish and host rock were also tested for the determination of standard electrochemical energy of activation ($\Delta H_{el}^{o\neq}$), standard entropy of activation ($\Delta S^{o\neq}$), and standard enthalpy of activation ($\Delta H^{o\neq}$). With this motive, an anodic polarization curve was recorded at different temperatures ranging from 25 to 55 °C in 1 M KOH (Fig. 13a and b). During the operation of this experiment, the temperature of the reference electrode was kept constant (25 ± 2 °C). Current density data was noted with each curve at a particular potential, and an Arrhenius plot, log i *vs.* 1/T (Fig. 13c), was constructed. The value of $\Delta H_{el}^{o\neq}$ was calculated by measuring the slope of the straight line obtained in the Arrhenius plot and is given in Table 6. As expected, the value of electrochemical activation energy for rock varnish is observed to be lower as compared to the host rock. The average value of α determined by the relation, $\alpha = 2.303RT/bF$, was almost unity with both electrocatalysts. Other thermodynamic parameters, such as standard entropy of activation ($\Delta S^{o\neq}$) and standard enthalpy of activation ($\Delta H^{o\neq}$) were obtained at different temperatures by using the relations (1) and (2) (ref. 122) and average values are listed in Table 6.

$$\Delta H_{el}^{o\neq} = \Delta H^{o\neq} - \alpha F\eta \quad (1)$$

$$\Delta S^{o\neq} = 2.3R\left[\log j + \frac{\Delta H_{el}^{o\neq}}{2.3RT} - \log(nF\omega C_{OH^-})\right] \quad (2)$$

where α (=2.303RT/bF) is the transfer coefficient. R, F, and T are the gas constant, Faraday constant, and absolute temperature, respectively, 'b' is the Tafel slope (in mV decade^{-1}) determined from the polarization curve recorded at different temperatures. The frequency term ω is equal to k_BT/h, where k_B and h are the Boltzmann constant and Planck's constant, respectively. The exceedingly negative value of $\Delta S^{o\neq}$ evinces the preamble of adsorption phenomena for the formation of oxygen electrochemically.

3.2.3 Mechanism. The XRF analysis reveals that Mn is the primary species in the rock varnish for OER. However, in the case of the host rock, Fe profusion dominates the OER. As a result, two approaches were proposed to explain OER on rock varnish and host rock based on the observed electrode kinetic (Tafel slope and reaction order) data.

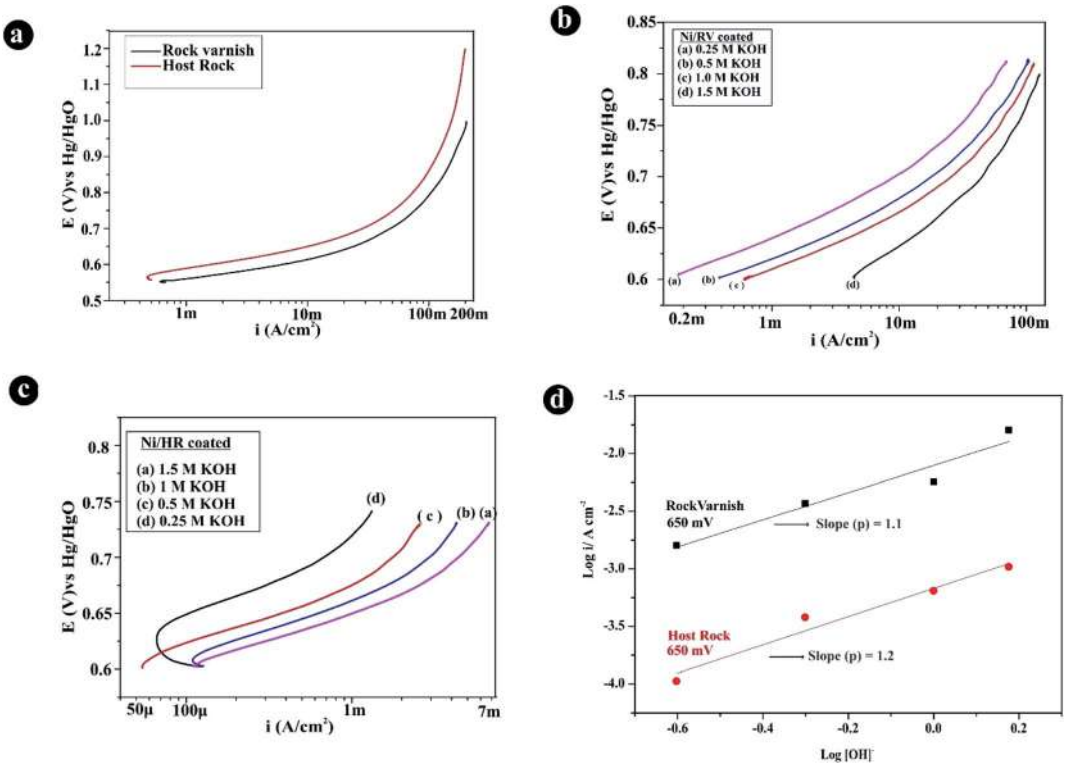

Fig. 12 (a) Tafel plots for oxygen evolution on the rock varnish film and host rock on Ni at 25 °C in 1 M KOH; (b) Tafel plots for oxygen evolution on the rock varnish on Ni at varying KOH concentrations ($\mu = 1.5$) at 25 °C; (c) Tafel plots for oxygen evolution on the host rock on Ni at varying KOH concentrations ($\mu = 1.5$) at 25 °C; (d) plot of log *i vs.* log[OH^-] at a constant applied potential ($E = 650$ mV) for rock varnish film and host rock on Ni at 25 °C depicting a first order process.

Scheme I: consider the O'Grady's path[123,124] for the OER.

$$S^z + OH^- \underset{k_{-1}}{\overset{k_1}{\rightleftharpoons}} S^zOH + e^- \quad (3)$$

$$S^zOH \underset{k_{-2}}{\overset{k_2}{\rightleftharpoons}} S^{z+1}OH + e^- \quad (4)$$

$$2S^{z+1}OH + 2OH^- \xrightarrow{k_3} 2S^z + H_2O + O_2 \quad (5)$$

where S^z is the active sites at the electrode surface.

Considering reaction (4) as the rate determining step, the overall rate under the Langmuir adsorption condition (when surface coverage, $\theta \rightarrow 0$) is given by;

$$v = k_2K_1C_{OH^-} \exp\left[\frac{(1+\beta)FE}{RT}\right] \quad (6)$$

where $K_1(=k_1/k_{-1})$ is the equilibrium constant for the adsorption–desorption process of step (1). β is the symmetry factor. The overall current density of the reaction is;

$$j = nFv$$

or

$$j = nFk_2K_1C_{OH^-} \exp\left[\frac{(1+\beta)FE}{RT}\right] \quad (7)$$

Assuming, $\beta = 1/2$;

The

$$\text{Tafel slope} = \frac{\partial E}{\partial(\log j)} = \frac{2.303\ RT}{\left(1+\frac{1}{2}\right)F} = \frac{2\times 2.303\ RT}{3F}$$

$= \sim 40$ mV per decade and reaction order $= \left[\frac{\partial(\log j)}{\partial(\log C_{OH^-})}\right]_E = 1$.

The Tafel slope and reaction order obtained from the above proposed mechanism are well in accord with the observed data with rock varnish (Tafel slope = 46 mV per decade and reaction order = ~1).

Scheme II: considering the path proposed by Krasil'shchikov.[125]

$$S + OH^- \underset{k_{-4}}{\overset{k_4}{\rightleftharpoons}} SOH + e^- \quad (8)$$

$$SOH + OH^- \underset{k_{-5}}{\overset{k_5}{\rightleftharpoons}} MO + H_2O + e^- \quad (9)$$

$$2MO \xrightarrow{k_6} 2M + O_2 \quad (10)$$

Assuming total surface coverage, $\theta \rightarrow 1$ under Langmuir adsorption condition, the rate determining step, eqn (9) gives;

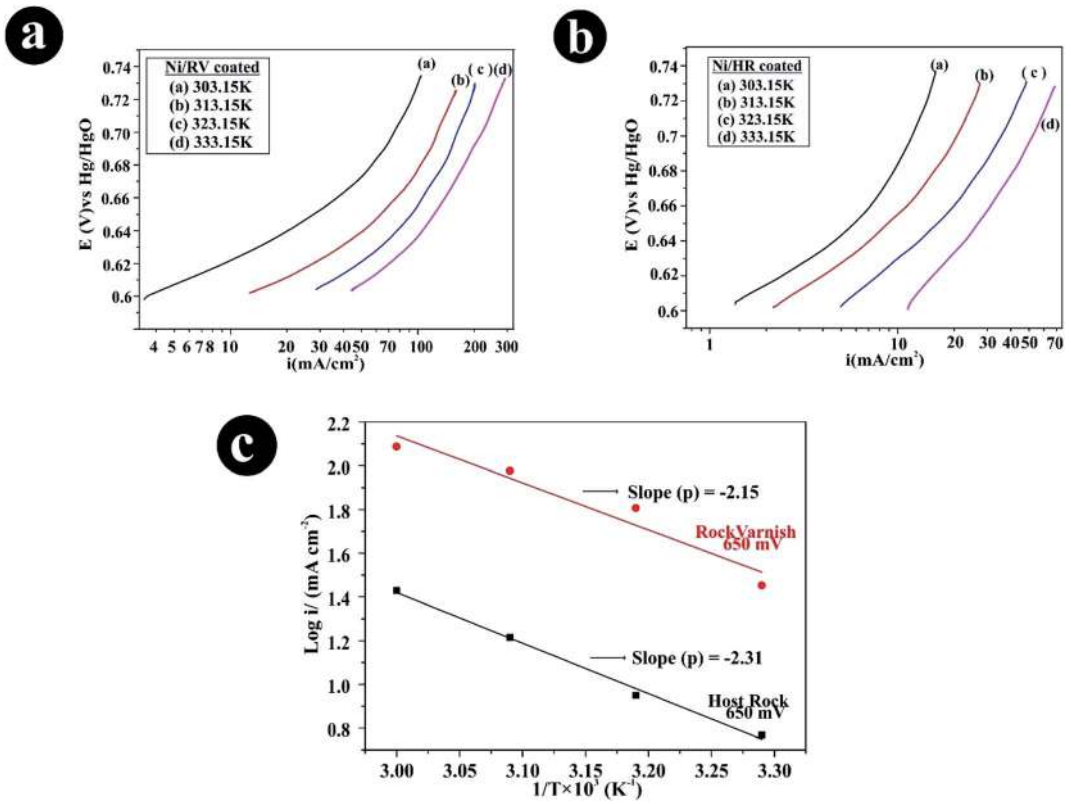

Fig. 13 (a) Tafel plots for oxygen evolution on the rock varnish film coated on Ni at different temperatures in 1 M KOH; (b) Tafel plots for oxygen evolution on host rock coated on Ni at different temperatures in 1 M KOH; (c) the Arrhenius plot at 650 mV applied potentials on rock varnish and host rock in 1 M KOH.

Table 6 Thermodynamic parameters for OER on rock varnish and host rock in 1 M KOH

Electrodes	$\Delta H_{el}^{0\#}$ (kJ mol^{-1}) at $E = 650$ mV	$-\Delta S^{0\#}$ (J deg^{-1} mol^{-1})	α	$\Delta H^{0\#}$ (kJ mol^{-1})
Ni/host rock	44.2	139.8 ± 6.6	0.80 ± 0.20	70.4 ± 7.5
Ni/rock varnish	41.2	129.9 ± 6.3	0.99 ± 0.27	74.4 ± 9.0

$$j = nFk_5K_4C_{OH^-}\exp\left(\frac{FE}{RT}\right) \quad (11)$$

where $K_4(=k_4/k_{-4})$ is the equilibrium constant for the adsorption–desorption process of eqn (8). Eqn (11) gives Tafel slope = 60 mV per decade and reaction order = 1, which resembles the data obtained with the host rock (Tafel slope = 52 mV per decade and reaction order = 1.2).

The above-mentioned mechanism, which takes both Tafel slope and reaction order into account, implies that the observed Tafel slope and reaction order on rock varnish for OER is contributed by eqn (3), in which adsorption and desorption of OH^- ions through the surface of the electrocatalyst plays an important role.

4. Conclusion

In summary, we have described hitherto unknown properties of the natural material rock varnish, which can be utilised as an electrocatalyst for active oxygen evolution reactions in alkaline media. Birnessite and clay minerals have been found in the varnish layer's complex moiety of related silicates and quartz, according to physicochemical analyses. The presence of clay minerals in the varnish material enhances the electrocatalytic quality of this material as an electrocatalyst by allowing considerable volumes of hydroxyl ions to adsorb and desorb on the catalyst surfaces, which in turn determines its reaction pathway and rate. As a result, its OER activity is significantly higher and superlative. The natural material's lower electrochemical activation energy, Tafel slope, and overpotential values push it towards an optimal electrocatalyst candidate. Our research not only opens new avenues to fundamentally synthesizing novel MnO_2-clay type composite materials by taking inspiration from this natural rock varnish material, but it also aids in the development of highly capable OER catalysts for extensive viable water splitting operations, thereby meeting our current and future clean and efficient energy needs.

Author contributions

A. S. C. performed formal analysis, conceptualization, data curation, and writing original draft, reviewing and editing the manuscript. N. K. S. contributed discussion on content related to electrochemical measurements and reviewing of the manuscript. M. M. performed impedance studies. A. S. contributed to the collection of samples, reviewing of the manuscript. N. K. S. and A. S. supervised this work.

Conflicts of interest

The authors declare no competing interests.

Acknowledgements

The work presented in the manuscript is part of the Ph.D. thesis work of A. S. C. We thank the Director, BSIP, for providing all necessary support for the work, which is carried out in the BSIP Laboratory; therefore, we particularly thank the BSIP-SAIF Facility. The experimental work was also carried out in the Department of Chemistry, University of Lucknow. N. K. S. is grateful to SERB (DST), New Delhi, for providing an electrochemical work station under the Fast-Track Scheme for Young Scientists (No.: SR/FT/CS-044/2009). We thank the Editor, Prof. Ryu Abe, in particular, for constructive recommendations and advice in creating better versions of the figures, as well as the anonymous reviewers for their useful remarks, which enhanced the initial versions of the paper during revisions.

References

1 R. I. Dorn, *Nature*, 1984, **310**, 767–770.
2 R. I. Dorn and T. M. Oberlander, *Progress in Physical Geography: Earth and Environment*, 1982, **6**, 317–367.
3 R. I. Dorn and D. H. Krinsley, *Geosciences*, 2019, **9**, 121.
4 W. S. Broecker and T. Liu, *GSA Today*, 2001, **7**, 4.
5 R. I. Dorn and N. Meek, *Earth Surf. Processes Landforms*, 1995, **20**, 547–560.
6 B. E. DiGregorio, *Anal. Chem.*, 2005, **77**, 433A–438A.
7 R. I. Dorn, in *Geomorphology of Desert Environments*, ed. A. J. Parsons and A. D. Abrahams, Springer Netherlands, Dordrecht, 2009, pp. 657–673.
8 P. U. Martínez-Pabello, C. Villalobos, S. Sedov, E. Solleiro-Rebolledo, J. Solé, T. Pi-Puig, B. Chávez-Vergara, J. Díaz-Ortega and A. Gubin, *Quaternary International*, 2021, **572**, 74–87.
9 G. Ren, Y. Yan, Y. Nie, A. Lu, X. Wu, Y. Li, C. Wang and H. Ding, *Front. Microbiol.*, 2019, **10**, 293.
10 A. U. Ubale, M. A. Waghmare, K. S. Iqbal and H. M. Pathan, *J. Mater. Sci.: Mater. Electron.*, 2020, **31**, 14003–14021.
11 M. Nitta, *Appl. Catal.*, 1984, **9**, 151–176.
12 Q. Feng, H. Kanoh and K. Ooi, *J. Mater. Chem.*, 1999, **9**, 319–333.
13 T. Abe and M. Kaneko, *Prog. Polym. Sci.*, 2003, **28**, 1441–1488.
14 K. Murofushi, K. Ogawa, H. Suzuki, R. Sakamoto, O. Tomita, K. Kato, A. Yamakata, A. Saeki and R. Abe, *J. Mater. Chem. A*, 2021, **9**, 11718–11725.
15 M. Higashi, K. Domen and R. Abe, *J. Am. Chem. Soc.*, 2013, **135**, 10238–10241.
16 S. Wang, A. Lu and C.-J. Zhong, *Nano Convergence*, 2021, **8**, 4.
17 S. Shiva Kumar and V. Himabindu, *Mater. Sci. Energy Technol.*, 2019, **2**, 442–454.
18 W.-H. Huang, X.-M. Li, X.-F. Yang, H.-B. Zhang, F. Wang and J. Zhang, *Chem. Commun.*, 2021, **57**, 4847–4850.
19 G. Zhao, K. Rui, S. X. Dou and W. Sun, *J. Mater. Chem. A*, 2020, **8**, 6393–6405.
20 Y. Lee, J. Suntivich, K. J. May, E. E. Perry and Y. Shao-Horn, *J. Phys. Chem. Lett.*, 2012, **3**, 399–404.
21 A. Grimaud, K. J. May, C. E. Carlton, Y.-L. Lee, M. Risch, W. T. Hong, J. Zhou and Y. Shao-Horn, *Nat. Commun.*, 2013, **4**, 2439.
22 A. Grimaud, O. Diaz-Morales, B. Han, W. T. Hong, Y.-L. Lee, L. Giordano, K. A. Stoerzinger, M. T. M. Koper and Y. Shao-Horn, *Nat. Chem.*, 2017, **9**, 457–465.
23 J. Hwang, R. R. Rao, L. Giordano, Y. Katayama, Y. Yu and Y. Shao-Horn, *Science*, 2017, **358**, 751–756.
24 S. Park, Y. H. Lee, S. Choi, H. Seo, M. Y. Lee, M. Balamurugan and K. T. Nam, *Energy Environ. Sci.*, 2020, **13**, 2310–2340.
25 Y.-Z. Wu, Y. Ding, T. Hayat, A. Alsaedi and S.-Y. Dai, *Appl. Surf. Sci.*, 2018, **459**, 430–437.
26 X.-F. Luo, J. Wang, Z.-S. Liang, S.-Z. Chen, Z.-L. Liu and C.-W. Xu, *Int. J. Hydrogen Energy*, 2017, **42**, 7151–7157.
27 G.-Q. Han, Y.-R. Liu, W.-H. Hu, B. Dong, X. Li, X. Shang, Y.-M. Chai, Y.-Q. Liu and C.-G. Liu, *J. Electrochem. Soc.*, 2015, **163**, H67.
28 J. Kim, J. S. Kim, H. Baik, K. Kang and K. Lee, *RSC Adv.*, 2016, **6**, 26535–26539.
29 K. Selvakumar, S. M. Senthil Kumar, R. Thangamuthu, G. Kruthika and P. Murugan, *Int. J. Hydrogen Energy*, 2014, **39**, 21024–21036.
30 H. Sim, J. Lee, T. Yu and B. Lim, *Korean J. Chem. Eng.*, 2018, **35**, 257–262.
31 M. Kölbach, S. Fiechter, R. van de Krol and P. Bogdanoff, *Catal. Today*, 2017, **290**, 2–9.
32 A. Ramírez, P. Hillebrand, D. Stellmach, M. M. May, P. Bogdanoff and S. Fiechter, *J. Phys. Chem. C*, 2014, **118**, 14073–14081.
33 L. Tian, J. Wang, K. Wang, H. Wo, X. Wang, W. Zhuang, T. Li and X. Du, *Carbon*, 2019, **143**, 457–466.
34 Z. Morgan Chan, D. A. Kitchaev, J. Nelson Weker, C. Schnedermann, K. Lim, G. Ceder, W. Tumas, M. F. Toney and D. G. Nocera, *Proc. Natl. Acad. Sci. U. S. A.*, 2018, **115**(23), E5261–E5268.
35 J. Orehotsky, H. Huang, C. R. Davidson and S. Srinivasan, *J. Electroanal. Chem. Interfacial Electrochem.*, 1979, **95**, 233–235.
36 C. Iwakura, M. Nishioka and H. Tamura, *Nippon Kagaku Kaishi*, 1982, 1136–1140.

37 R. N. Singh, N. K. Singh, J. P. Singh, G. Balaji and N. S. Gajbhiye, *Int. J. Hydrogen Energy*, 2006, **31**, 701–707.
38 R. N. Singh, J. P. Pandey, N. K. Singh, B. Lal, P. Chartier and J.-F. Koenig, *Electrochim. Acta*, 2000, **45**, 1911–1919.
39 N. K. Singh, J. P. Singh and R. N. Singh, *Int. J. Hydrogen Energy*, 2002, **27**, 895–903.
40 Z. Zhang, D. Zhou, X. Wu, X. Bao, J. Liao and M. Wen, *Int. J. Hydrogen Energy*, 2019, **44**, 7222–7227.
41 B. Shin, S. Choi and Y. Tak, *Int. J. Electrochem. Sci.*, 2016, **11**, 5900–5908.
42 H. M. Rietveld, *J. Appl. Crystallogr.*, 1969, **2**, 65–71.
43 T. Degen, M. Sadki, E. Bron, U. König and G. Nénert, *Powder Diffr.*, 2014, **29**, S13–S18.
44 K. Momma and F. Izumi, *J. Appl. Crystallogr.*, 2011, **44**, 1272–1276.
45 R. N. Singh, S. K. Tiwari, S. P. Singh, N. K. Singh, G. Poillerat and P. Chartier, *J. Chem. Soc., Faraday Trans.*, 1996, **92**, 2593–2597.
46 S. K. Tiwari, J. F. Koenig, G. Poillerat, P. Chartier and R. N. Singh, *J. Appl. Electrochem.*, 1998, **28**, 114–119.
47 Y.-K. Hsu, Y.-C. Chen, Y.-G. Lin, L.-C. Chen and K.-H. Chen, *J. Mater. Chem.*, 2012, **22**, 2733–2739.
48 N. K. Singh, P. Sharma, I. kumar and A. S. Chaddha, *Int. J. Electrochem. Sci.*, 2019, 11379–11390.
49 S. L. Candelaria, N. M. Bedford, T. J. Woehl, N. S. Rentz, A. R. Showalter, S. Pylypenko, B. A. Bunker, S. Lee, B. Reinhart, Y. Ren, S. P. Ertem, E. B. Coughlin, N. A. Sather, J. L. Horan, A. M. Herring and L. F. Greenlee, *ACS Catal.*, 2017, **7**, 365–379.
50 M. E. Brookfield and C. P. Andrews-Speed, *Sediment. Geol.*, 1984, **40**, 249–286.
51 M. P. Searle, *J. Struct. Geol.*, 1986, **8**, 923–936.
52 J. Y. Shin, C. M. Buzgo and M. A. Cheney, *Colloids Surf., A*, 2000, **172**, 113–123.
53 Z. Y. Leong and H. Y. Yang, *ACS Appl. Mater. Interfaces*, 2019, **11**, 13176–13184.
54 C. Wei, L. Yu, C. Cui, J. Lin, C. Wei, N. Mathews, F. Huo, T. Sritharan and Z. Xu, *Chem. Commun.*, 2014, **50**, 7885–7888.
55 Y. M. Mos, A. C. Vermeulen, C. J. N. Buisman and J. Weijma, *Geomicrobiol. J.*, 2018, **35**, 511–517.
56 E. P. Vicenzi, C. A. Grissom, R. A. Livingston and Z. Weldon-Yochim, *Heritage Sci.*, 2016, **4**, 26.
57 N. P. Arias, M. E. Becerra and O. Giraldo, *Nanomater.*, 2019, **9**, 1156.
58 R. T. Cygan, J. E. Post, P. J. Heaney and J. D. Kubicki, *Am. Mineral.*, 2012, **97**, 1505–1514.
59 S. Boyd, K. Ganeshan, W.-Y. Tsai, T. Wu, S. Saeed, D. Jiang, N. Balke, A. C. T. van Duin and V. Augustyn, *Nat. Mater.*, 2021, **20**, 1689–1694.
60 X.-Z. Zhai, J. Qu, S.-M. Hao, Y.-Q. Jing, W. Chang, J. Wang, W. Li, Y. Abdelkrim, H. Yuan and Z.-Z. Yu, *Nano-Micro Lett.*, 2020, **12**, 56.
61 A. Zhang, B. Mu, X. Wang, L. Wen and A. Wang, *Front. Chem.*, 2018, **6**, 125.
62 D. S. Yang and M. K. Wang, *Chem. Mater.*, 2001, **13**, 2589–2594.
63 A.-C. Gaillot, D. Flot, V. A. Drits, A. Manceau, M. Burghammer and B. Lanson, *Chem. Mater.*, 2003, **15**, 4666–4678.
64 S. L. Brock, N. Duan, Z. R. Tian, O. Giraldo, H. Zhou and S. L. Suib, *Chem. Mater.*, 1998, **10**, 2619–2628.
65 L. Yang, S. Cheng, J. Wang, X. Ji, Y. Jiang, M. Yao, P. Wu, M. Wang, J. Zhou and M. Liu, *Nano Energy*, 2016, **30**, 293–302.
66 X. Xu, Y. Li, Y. Li, A. Lu, R. Qiao, K. Liu, H. Ding and C. Wang, *Chem. Geol.*, 2019, **522**, 55–70.
67 R. J. Hemley, in *High-Pressure Research in Mineral Physics: A Volume in Honor of Syun-iti Akimoto*, American Geophysical Union (AGU), 1987, pp. 347–359.
68 C. Malherbe, R. Ingley, I. Hutchinson, H. Edwards, A. S. Carr, L. Harris and A. Boom, *Astrobiology*, 2015, **15**, 442–452.
69 X. Fu, A. Wang and M. J. Krawczynski, *J. Geophys. Res.*, 2017, **122**, 839–855.
70 E. J. Israel, R. E. Arvidson, A. Wang, J. D. Pasteris and B. L. Jolliff, *J. Geophys. Res.*, 1997, **102**, 28705–28716.
71 J. A. Gadsden, *Infrared spectra of minerals and related inorganic compounds*, Butterworths, London, 1975.
72 J. Luo, Q. Zhang, A. Huang, O. Giraldo and S. L. Suib, *Inorg. Chem.*, 1999, **38**, 6106–6113.
73 R. M. Potter and G. R. Rossman, *Am. Mineral.*, 1979, **64**, 1199–1218.
74 N. V. Chukanov, *Infrared spectra of mineral species: extended library*, Springer Science & Business Media, 2013.
75 S. Min and Y. Kim, *Minerals*, 2020, **10**, 884.
76 R. M. Potter and G. R. Rossman, *Science*, 1977, **196**, 1446–1448.
77 M. J. R. Halstead, R. G. Cunninghame and K. A. Hunter, *Atmos. Environ.*, 2000, **34**, 665–676.
78 R. A. Sutherland, *Environ. Geol.*, 2000, **39**, 611–627.
79 R. L. Rudnick and S. Gao, in *Treatise on Geochemistry*, Elsevier, 2003, pp. 1–64.
80 J. A. Barrat, B. Zanda, F. Moynier, C. Bollinger, C. Liorzou and G. Bayon, *Geochim. Cosmochim. Acta*, 2012, **83**, 79–92.
81 S. M. McLennan, *Geochem., Geophys., Geosyst.*, 2001, **2**, 2000GC000109.
82 I. Spanos, J. Masa, A. Zeradjanin and R. Schlögl, *Catal. Lett.*, 2021, **151**, 1843–1856.
83 X. Tan, F. Liu, L. Hu, A. H. Reed, Y. Furukawa and G. Zhang, *Appl. Clay Sci.*, 2017, **135**, 313–324.
84 C. D. Hatch, J. S. Wiese, C. C. Crane, K. J. Harris, H. G. Kloss and J. Baltrusaitis, *Langmuir*, 2012, **28**, 1790–1803.
85 W. R. Schell and J. V. Jordan, *Plant Soil*, 1959, **10**, 303–318.
86 N. Jiang, X. Liu, J. Dong, B. You, X. Liu and Y. Sun, *ChemNanoMat*, 2017, **3**, 491–495.
87 M. S. Ali Akbari, R. Bagheri, Z. Song and M. M. Najafpour, *Sci. Rep.*, 2020, **10**, 8757.
88 P. Ganesan, A. Sivanantham and S. Shanmugam, *J. Mater. Chem. A*, 2016, **4**, 16394–16402.
89 M. Łuba, T. Mikołajczyk, M. Kuczyński, B. Pierożyński and I. M. Kowalski, *Catalysts*, 2021, **11**, 468.
90 E. Cossar, A. Oyarce Barnett, F. Seland and E. A. Baranova, *Catalysts*, 2019, **9**, 814.

91 Y. Tian, Q. Wang, Z. Peng, S. Guan and X. Fu, *Molecules*, 2021, **26**, 4517.
92 O. Diaz-Morales, F. Calle-Vallejo, C. de Munck and M. T. M. Koper, *Chem. Sci.*, 2013, **4**, 2334–2343.
93 J. Willsau, O. Wolter and J. Heitbaum, *J. Electroanal. Chem. Interfacial Electrochem.*, 1985, **195**, 299–306.
94 N. K. Singh, S. K. Tiwari, K. L. Anitha and R. N. Singh, *J. Chem. Soc., Faraday Trans.*, 1996, **92**, 2397–2400.
95 S. K. Tiwari, P. Chartier and R. N. Singh, *J. Electrochem. Soc.*, 1995, **142**, 148–153.
96 Q. Kang, L. Vernisse, R. C. Remsing, A. C. Thenuwara, S. L. Shumlas, I. G. McKendry, M. L. Klein, E. Borguet, M. J. Zdilla and D. R. Strongin, *Effect of Interlayer Spacing on the Activity of Layered Manganese Oxide Bilayer Catalysts for the Oxygen Evolution Reaction*, **https://pubs.acs.org/doi/pdf/10.1021/jacs.6b09184**, accessed February 4, 2022.
97 T. Lim, M. Sung and J. Kim, *Sci. Rep.*, 2017, **7**, 15382.
98 A. S. Chaddha, A. Sharma and N. K. Singh, *MethodsX*, 2021, **8**, 101511.
99 D. M. Morales, M. A. Kazakova, S. Dieckhöfer, A. G. Selyutin, G. V. Golubtsov, W. Schuhmann and J. Masa, *Adv. Funct. Mater.*, 2020, **30**, 1905992.
100 C. C. L. McCrory, S. Jung, J. C. Peters and T. F. Jaramillo, *J. Am. Chem. Soc.*, 2013, **135**, 16977–16987.
101 G.-Q. Han, X. Li, X. Zhao, B. Dong, W.-H. Hu, Y.-R. Liu, X. Shang, Y.-M. Chai and C.-G. Liu, *J. Solid State Electrochem.*, 2016, **20**, 2907–2912.
102 P.-P. Liu, Y.-Q. Zheng, H.-L. Zhu and T.-T. Li, *ACS Appl. Nano Mater.*, 2019, **2**, 744–749.
103 M. Q. Yu, Y. H. Li, S. Yang, P. F. Liu, L. F. Pan, L. Zhang and H. G. Yang, *J. Mater. Chem. A*, 2015, **3**, 14101–14104.
104 Y. Zhao, J. Zhang, W. Wu, X. Guo, P. Xiong, H. Liu and G. Wang, *Nano Energy*, 2018, **54**, 129–137.
105 K. Fujimoto, T. Okada and M. Nakayama, *J. Phys. Chem. C*, 2018, **122**, 8406–8413.
106 Z. Ye, T. Li, G. Ma, Y. Dong and X. Zhou, *Adv. Funct. Mater.*, 2017, **27**, 1704083.
107 Q. Kang, L. Vernisse, R. C. Remsing, A. C. Thenuwara, S. L. Shumlas, I. G. McKendry, M. L. Klein, E. Borguet, M. J. Zdilla and D. R. Strongin, *J. Am. Chem. Soc.*, 2017, **139**, 1863–1870.
108 H. Antoni, D. M. Morales, J. Bitzer, Q. Fu, Y.-T. Chen, J. Masa, W. Kleist, W. Schuhmann and M. Muhler, *J. Catal.*, 2019, **374**, 335–344.
109 E. Jung, J. K. Kim, H. Choi, M. H. Lee and T. Yu, *Dalton Trans.*, 2018, **47**, 17342–17348.
110 V. Maruthapandian, T. Pandiarajan, V. Saraswathy and S. Muralidharan, *RSC Adv.*, 2016, **6**, 48995–49002.
111 H. Xue, H. Yu, Y. Li, K. Deng, Y. Xu, X. Li, H. Wang and L. Wang, *Nanotechnology*, 2018, **29**, 285401.
112 Q. Hu, X. Liu, B. Zhu, G. Li, L. Fan, X. Chai, Q. Zhang, J. Liu and C. He, *J. Power Sources*, 2018, **398**, 159–166.
113 K.-L. Yan, X. Shang, W.-K. Gao, B. Dong, X. Li, J.-Q. Chi, Y.-R. Liu, Y.-M. Chai and C.-G. Liu, *J. Alloys Compd.*, 2017, **719**, 314–321.
114 J.-H. Zhang, J.-Y. Feng, T. Zhu, Z.-L. Liu, Q.-Y. Li, S.-Z. Chen and C.-W. Xu, *Electrochim. Acta*, 2016, **196**, 661–669.
115 C. Hu, L. Zhang, Z. Huang, W. Zhu, Z.-J. Zhao and J. Gong, *J. Catal.*, 2019, **369**, 105–110.
116 M. Li, L. Bai, X. Wen and J. Guan, *Int. J. Hydrogen Energy*, 2018, **43**, 15807–15814.
117 Y. Han, Y. Yu, L. Zhang, L. Huang, J. Zhai and S. Dong, *Talanta*, 2018, **186**, 154–161.
118 X. Xiong, Y. Ji, M. Xie, C. You, L. Yang, Z. Liu, A. M. Asiri and X. Sun, *Electrochem. Commun.*, 2018, **86**, 161–165.
119 J. He, M. Wang, W. Wang, R. Miao, W. Zhong, S.-Y. Chen, S. Poges, T. Jafari, W. Song, J. Liu and S. L. Suib, *ACS Appl. Mater. Interfaces*, 2017, **9**, 42676–42687.
120 L. Li, J. Yang, H. Yang, L. Zhang, J. Shao, W. Huang, B. Liu and X. Dong, *ACS Appl. Energy Mater.*, 2018, **1**, 963–969.
121 C. Guo, Y. Zheng, J. Ran, F. Xie, M. Jaroniec and S.-Z. Qiao, *Angew. Chem., Int. Ed.*, 2017, **56**, 8539–8543.
122 E. Gileadi, *Electrode kinetics for chemists, chemical engineers and material scientists*, VCH, Weinheim, New York, 1993, 151.
123 W. O'Grady, C. Iwakura, J. Huang and E. Yeager, *Proceedings of the Symposium on Electrocatalysis,* ed. M. W. Breiter, The Electrochemical Society Inc., Pennington, NJ, 1974.
124 H. Dau, C. Limberg, T. Reier, M. Risch, S. Roggan and P. Strasser, *ChemCatChem*, 2010, **2**, 724–761.
125 A. I. Krasil'shchikov, *Zh. Fiz. Khim.*, 1963, **37**, 531–537.